

In situ SEM Observation of Column-like and Foam-like CNT Array Nanoindentation

Matthew R. Maschmann,^{†,‡} QiuHong Zhang,^{†,§} Robert Wheeler,[†] Feng Du,[#] Liming Dai,[#] and Jeffery Baur^{*,†}

[†] Air Force Research Laboratory, Materials and Manufacturing Directorate, AFRL/RX, Wright-Patterson Air Force Base, Ohio 45433, United States

[‡] Universal Technology Corporation, Beavercreek, Ohio 45432, United States

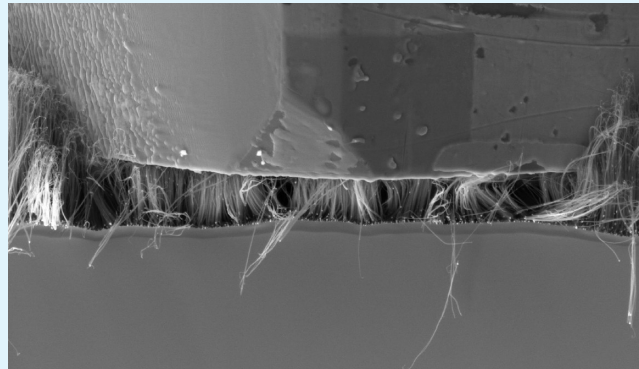
[§] University of Dayton Research Institute, University of Dayton, Dayton, Ohio 45469, United States

[#] UES Inc., Dayton, Ohio 45432, United States

^{*} Department of Chemical Engineering, Case Western University, Cleveland, Ohio, 44106

 Supporting Information

ABSTRACT: Quantitative nanoindentation of nominally 7.5 and 600 μm tall vertically aligned carbon nanotube (VACNT) arrays is observed *in situ* within an SEM chamber. The 7.5 μm array consists of highly aligned and weakly interacting CNTs and deflects similarly to classically defined cylindrical columns, with deformation geometry and critical buckling force well estimated using the Euler–Bernoulli theory. The 600 μm array has a highly entangled foam-like morphology and exhibits sequential buckle formation upon loading, with a buckle first forming near the array bottom at approximately 2% strain, followed by accumulating coordinated buckling at the top surface at strains exceeding 5%.



KEYWORDS: carbon nanotube, compression, indentation, buckling, *in situ* observation

The compressive response of VACNT arrays consists of complex phenomena occurring on multiple length scales. Their behavior is expected to rely heavily on the properties of individual constituent CNTs, interactions and load distribution between neighboring CNTs, and the distribution of these properties throughout the array. The understanding of VACNT array mechanics through compression and nanoindentation testing, however, is traditionally limited to examination of stress–strain relationships and post-mortem deformation analysis rather than real-time observation, allowing limited insight into the deformation mechanisms. Researchers have observed both remarkable elasticity^{1,2} and fatigue resistance² of VACNT arrays at strains up to 85%, whereas others report significant permanent plastic deformation even at modest strains.^{3–6} Deformed arrays may exhibit coordinated buckles and folds residing strictly on the bottom side of arrays,^{1,4,6} strictly on the top surface,³ a mixture of both,³ or neither.⁷ Because of lack of direct observation, competing theoretical frameworks have been advanced to explain specific CNT array mechanics attributes guided solely on interpretation of postdeformation analysis. Theoretical treatment of VACNT arrays as classical columns is frequent,^{4,7–9} often underpredicting the critical buckling load of arrays by orders of magnitude. Alternatively, open-cell foam models have also been proposed^{1,3,6,10} on the basis of analogous stress–strain behavior and similar morphology. Recently, the

first *in situ* SEM compression of lithographically defined 50 μm diameter VACNT cylinders of highly entangled morphology was demonstrated, providing the first direct observation of plastic bottom-to-top buckle formation in a compressed foam-like array.⁶ The report showed the efficacy of the *in situ* technique, though it is unclear how the findings will translate to CNTs of other morphologies. We report the *in situ* SEM nanoindentation of two distinct multiwalled VACNT array morphologies, namely a 7.5 μm well-aligned array with limited neighboring CNT interactions and a 600 μm tall array with a highly entangled morphology and their resulting beamlike deflection and foam-like buckling and crushing, respectively.

The nominally 7.5 μm tall silicon supported VACNT array was synthesized from pyrolysis of iron(II) phthalocyanine, producing vertically aligned CNTs with a nominal outer diameter of 50 nm.^{11,12} The array was indented using a $40 \times 40 \mu\text{m}$ diamond flat punch with 200 nm displacement intervals. As seen in Figure 1d, individual CNTs have limited interaction with neighbors due to their linear vertical orientation and modest aspect ratio. Initial loading during indentation testing leads to the angular shifting of a small fraction of observable CNTs and some localized CNT tip

Received: December 22, 2010

Accepted: February 25, 2011

Published: March 02, 2011

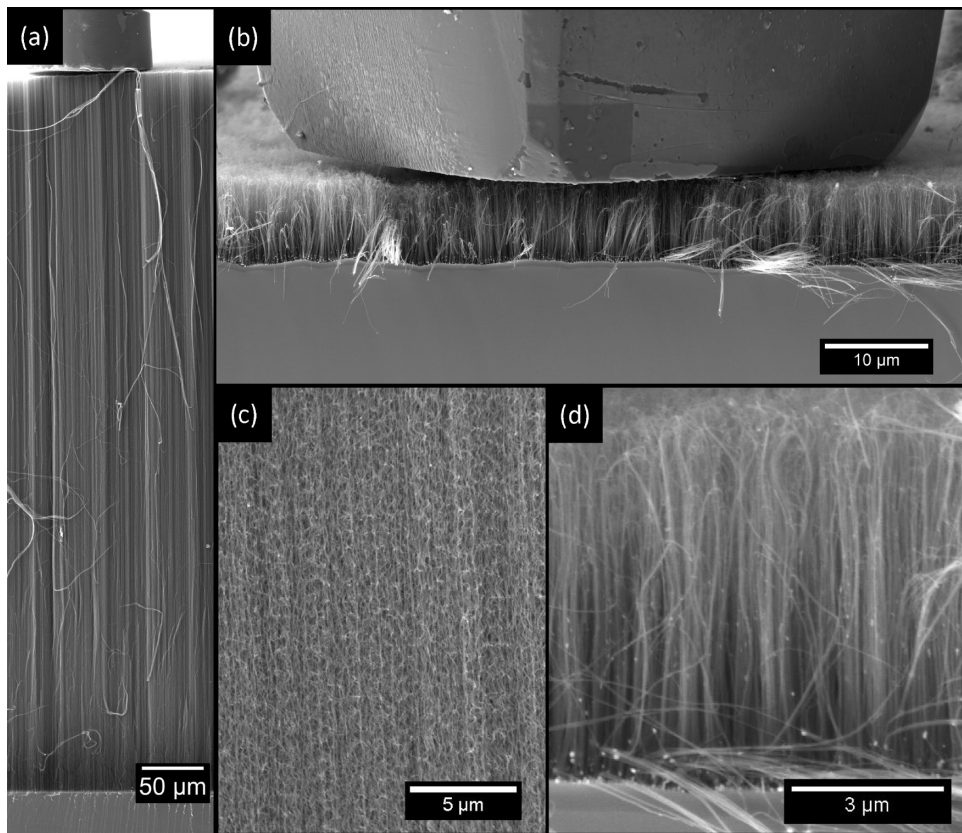


Figure 1. Initial CNT array morphology. Low-magnification SEM micrograph of (a) 600 μm array and (b) 7.5 μm array. High-magnification micrograph of (c) 600 μm array and (d) 7.5 μm array.

bending as load is applied to the CNTs. Loading to 20% strain results in localized top-side bending for a significant fraction of the observable CNTs, as observed in Figure 2a. The deformation geometry is similar in appearance to that anticipated by a column mechanically supported by pin-fixed boundary conditions, whereby the largest bending occurs between the pin support and an effective length of 70% the original column height. The localized bending deepens to a strain of 40–45%, followed by significant lateral motion within the observed portion of the CNT array, indicating yielding. Deflection orientations seem to couple among neighboring CNTs, creating localized areas of relative densification or decreased occupation as observed in Figure 2b. At very high strain above 60% (Figure 2b), the bottom segment of the yielded CNTs rotate or bend between the inflection point and the substrate. The amplitude of the bottom bending and rotation increases to the maximum applied strain of 90%, with negligible slippage observed between the indenter and the CNT tips (Figure 2c). Upon unloading the CNTs recover 80–90% of their original height (Figure 2d), though residual CNT curvature and some delamination are observed. The unloaded geometry bears strong resemblance to a classical compressed column with pin-fixed boundary conditions, shown schematically in Figure 2d. The line in the schematic represents the effective length of an equivalent classical column with pin-fixed boundary conditions, representing the location of zero bending moment. This height is a common inflection point in the observed CNTs, indicating that this location served as a location of zero moment, consistent with classical theory. A video of the indent shows the deflection sequence and may be found in the Supporting Information (Video S1).

The stress–strain relationship obtained from this indent, shown in Figure 3a, is linear from the initiation of contact to 45% strain (0.5 MPa stress), followed by a reduced slope indicative of a buckling event. This critical strain corresponds to the onset of buckling observed via SEM. At 75% strain the stress–strain slope increases dramatically, indicating an increased stiffness due to densification and the increasing influence of substrate mechanical properties. The unloading stroke exhibits hysteretic behavior, consistent with observations by others.^{3,6,7} It should be noted that strain is calculated relative to SEM image correlation to correct for slight stage drift during loading.

The observed column-like deformation is similar in appearance to classical column bending for which Euler–Bernoulli beam theory is employed to predict the critical buckling load. This load may be expressed as

$$F_{\text{cr}} = \frac{\pi^2 EI}{(KL)^2} \quad (1)$$

Where F_{cr} is the critical buckling load, E is the elastic modulus of the column, I is the column's second moment of inertia, K is a constant determined from boundary conditions, and L is the length of the column. The second moment of inertia for a hollow cylinders is expressed as

$$I = \frac{\pi(d_o^4 - d_i^4)}{64} \quad (2)$$

where d_o and d_i represent the outer and inner diameter of the cylinder, respectively. Based on observation and intuition, the

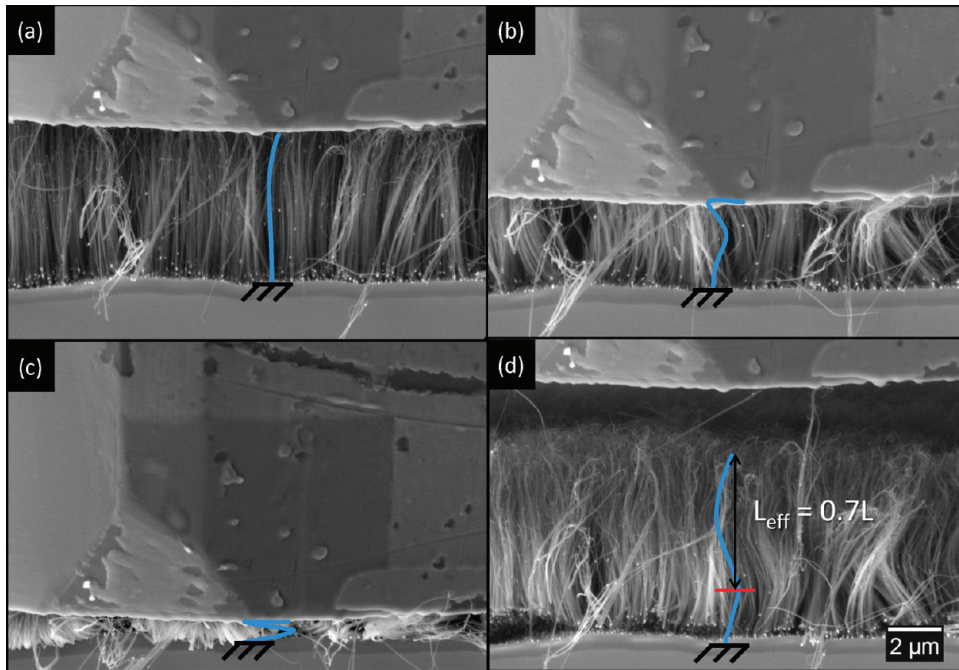


Figure 2. In situ observation of a $7.5\text{ }\mu\text{m}$ VACNT array at (a) 20% strain, (b) postbuckling at 60% strain, (c) maximum compression of 90% strain, and (d) upon full retraction of indenter tip. The blue line indicates the approximate contour of a single CNT.

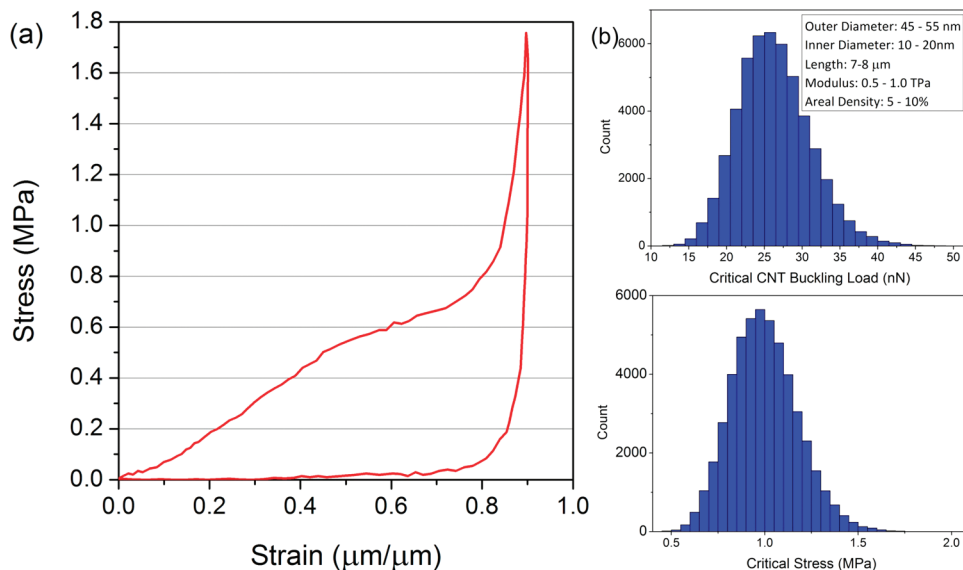


Figure 3. Nanoindentation of a $7.5\text{ }\mu\text{m}$ VACNT array. (a) Experimentally obtained stress-strain relationship and (b) Monte Carlo distributions for estimated critical buckling load of individual CNTs (top) and corresponding critical stress as measured by the indenter head (bottom).

mechanical support boundary conditions were chosen such that the free end may support loading but not a bending moment (pin condition), and the base of a CNT is fixed such that it may support both forces and bending moment, consistent with SEM observations. For these boundary conditions $K = 0.7$ in eq 1.

A Monte Carlo simulation was employed to estimate the critical buckling load for an ideal field of vertical hollow columns having distributed properties to account for natural variation of CNTs properties and uncertainty in measured and estimated properties. The distributed properties of length, outer diameter, and areal density were approximated based upon SEM observation. The

inner diameter distribution was estimated based on TEM analysis.^{11,12} For simplicity, normal distributions were assumed for all input parameters, with input distributions ranges representing six standard deviations displayed in Figure 3b. Input distributions include an outer diameter between 45 and 55 nm, inner diameter between 10 and 20 nm, length between 7 and 8 μm , and areal density between 5 and 10%. An elastic modulus distribution of 0.5–1.0 TPa was approximated based upon literature.^{13–16} On the basis of these inputs, the computed critical load distribution ranges from approximately 12–45 nN per CNT (25 nN mean), corresponding to approximately 0.5–1.6 MPa (1.0 MPa mean) critical

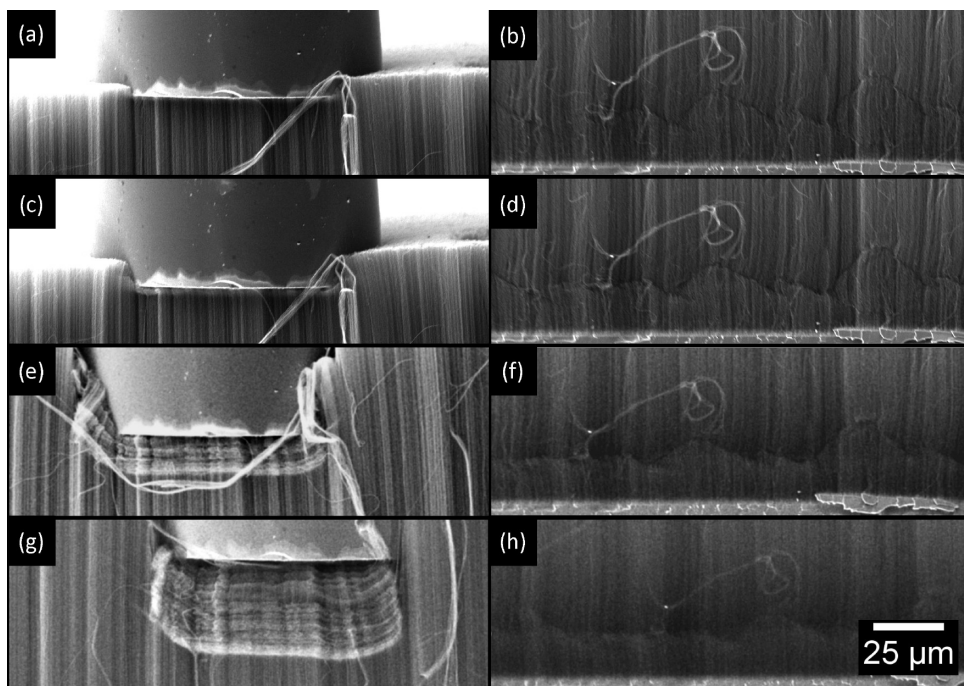


Figure 4. Sequential SEM micrographs showing the evolution of the top (left) and bottom (right) deformation of a $600\text{ }\mu\text{m}$ VACNT array indented with a $100\text{ }\mu\text{m}$ flat punch to strains of (a, b) 1.7% ($10\text{ }\mu\text{m}$), (c, d) 5% ($30\text{ }\mu\text{m}$), (e, f) 15% ($90\text{ }\mu\text{m}$), and (g, h) 22.5% ($135\text{ }\mu\text{m}$).

stress during indentation. The experimentally obtained critical stress of approximately 0.5 MPa is well approximated by the lower end of the predicted Monte Carlo distribution. Note that non-idealities such as slight angular misalignment of CNT and curved CNT free ends, which may decrease the critical loading of a portion of the indented CNTs, were not considered in the Monte Carlo analysis. The correlation between the Monte Carlo estimation and experimental results lends additional support to the validity of approximating the $7.5\text{ }\mu\text{m}$ CNT array as a field of classical vertical slender columns. The application of this model to arrays of similar morphology is anticipated to be valid assuming that individual CNTs within the array maintain a general vertical orientation without inherent waviness or strong neighbor-to-neighbor interactions.

The $600\text{ }\mu\text{m}$ VACNT array, synthesized using a Fe film catalyst,¹⁷ was indented using a custom $100\text{ }\mu\text{m}$ diameter SiC flat punch tip and $1\text{ }\mu\text{m}$ displacement increments to a maximum displacement of $45\text{ }\mu\text{m}$. The typical diameter range for CNTs within the array ranged from 10 to 15 nm, with 2–8 walls.³ Unlike the $7.5\text{ }\mu\text{m}$ array, individual CNTs exhibited significant waviness, interaction, and entanglement between neighboring CNTs (Figure 1c). The larger diameter and short span of the $7.5\text{ }\mu\text{m}$ array are believed to limit similar interactions between the CNTs in the previous array. Upon application of initial loading, a single buckle forms near the bottom of the array within the first 1.7% strain ($10\text{ }\mu\text{m}$), as observed in Figure 4b. Further compression deepens this bottom buckle, as the CNT region directly above translates downward and is drawn into the buckled area. The width of the bottom buckle exceeds the projection of the indenter cross section, indicating that the array may locally distribute the applied load laterally via neighboring interactions. Although buckle formation initiates near the array bottom, consistent with previous in situ observation of VACNT columns,⁶ additional progressive buckle formation at the bottom of the array is not observed. Rather, new

buckle formation is observed directly beneath the indenter tip near the top of the array at approximately 5% strain ($30\text{ }\mu\text{m}$), as observed in Figure 4c. This buckling region deepens with increased strain to the maximum strain of 7.5%, as subsequent additional buckles form an accumulating front underneath the indenter at approximately $3\text{--}5\text{ }\mu\text{m}$ intervals. Little deepening of the bottom-side buckle is observed during the accumulation of top-side buckles, as observed in Figures 4d–f. From 7.5% strain, all buckles are relieved upon release of load, and the array returns to its original height. Consequently, the localized buckling modes and their sequential evolution with strain would be difficult or impossible to ascertain in the absence of in situ observation. A video of this indent may be found in the Supporting Information (Video S2).

This observed deformation evolution is consistent with a qualitative model previously proposed, whereby the natural profile of vertical alignment and density of CNT morphology as a function of height^{18,19} relates to a corresponding similar profile of height-dependent yield strength.³ For a $600\text{ }\mu\text{m}$ array, the alignment and yield strength at the bottom of the array may be slightly less than that at the top of the array, but has been observed to increase rapidly with height above the substrate.¹⁸ As the site of lowest yield strength, the bottom of the array serves as the most likely site for buckle initiation. If buckling initiates, the stronger and denser region directly above the buckle translates downward, and the bottom layer is subsequently fortified with material of higher yield strength than that of both the original bottom and top side of the array. The region of lowest yield strength then transfers to the top of the array. In situ observations also reveal that stress tends to be laterally distributed to a width exceeding that of the indenter head (Figure 4b) near the bottom of the array but is confined to directly under the indenter tip near the top of the array. For these reasons, further buckling may be anticipated to originate and remain confined to the top surface unless the region of lowest yield stress is transferred to some other location within the array.

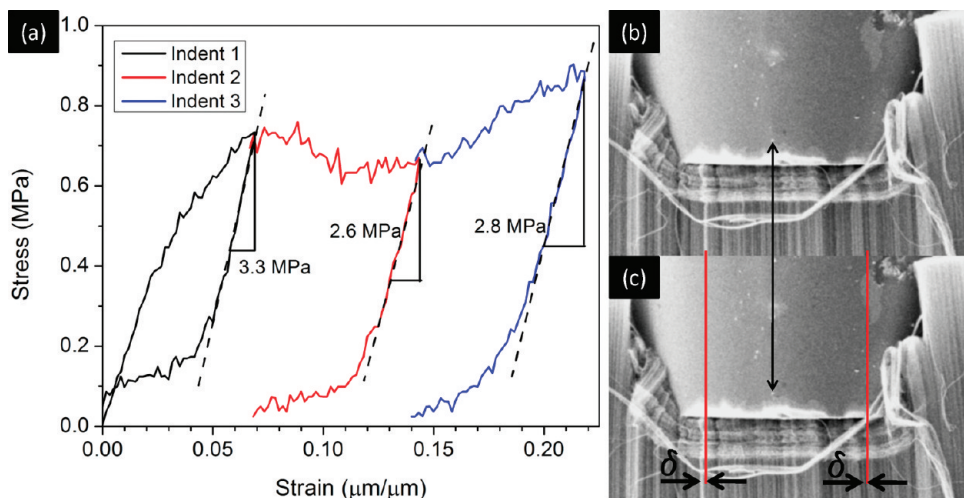


Figure 5. Nanoindentation of $600\text{ }\mu\text{m}$ VACNT array. (a) Stress–strain behavior, with dotted lines representing the unloading slope used to compute elastic modulus. Lateral motion, δ , of CNT array during new buckle formation is observed by comparing high contrast vertical CNT bundles as fiducial markers (b) prior to and (c) after buckling event. The red vertical lines represent the initial position of the tracked marker while the left-most arrow represents the postbuckled location of the marker.

Two additional indents to greater effective depths were performed at the same location. To accommodate an indent depth greater than $45\text{ }\mu\text{m}$, the indenter tip actuation stroke reinitialized to the top of its stroke, and the stage was translated $45\text{ }\mu\text{m}$ closer to the indenter tip between subsequent tests. Using this technique, the indenter head penetrates to a final strain of 22.5% ($135\text{ }\mu\text{m}$) through three sequential indents. Figures 4e–h display SEM micrographs obtained at various strains during the second and third indentations and represent individual frames from Supporting Information (Videos S2 and S3) which depict the indents in their entirety. Upon initiation of the second indentation at 7.5% initial strain, the accumulation of additional buckles at the top buckling front continues with additional applied strain, while little vertical translation or deepening of the bottom buckle is observed. The top buckling front proceeds downward under the projected cross-section of the indenter tip with little influence on the CNTs immediately neighboring the compacted buckling region observed. This observation seems to indicate that the more vertically aligned morphology near the top of the array inhibits lateral force distribution compared to the more disorganized morphology near bottom of the array. The top-side buckling front becomes sufficiently large that at 22.5% strain ($135\text{ }\mu\text{m}$) the front precedes the tip by a depth of approximately $40\text{ }\mu\text{m}$. Interestingly, the array exhibits significant lateral motion during formation of each new top buckle by tracking the naturally occurring high-contrast vertical CNT bundles as fiducial markers, as depicted in Figure 5b. This observation adds context to the lateral forces measured during nanoindentation of buckle formation in VACNT arrays of similar height and morphology³ and has also been recently observed during formation of bottom-side buckles.⁶ Upon final tip withdrawal the bottom buckle recovers significantly, whereas the top buckles retain their buckled configuration with little recovery. The permanent deformation of the top buckles may result from significant neighboring interactions within the compacted region because of localized densification and increased entanglement, whereas elastic recovery of the bottom buckle may similarly be due to lesser densification, entanglement, and relatively low local density.

The stress–strain plot of the $600\text{ }\mu\text{m}$ VACNT array nanoindentation in Figure 5a is consistent with that of an open-cell foam material.²⁰ An initial linear region exists for the initial 2% strain, followed by a region of slightly reducing slope. It is within this strain regime that the bottom buckle forms and grows. A dramatic slope decrease and subsequent plateau region forms between approximately 5–6% strain as top-side accumulating buckle formation begins to dominate the deformation. Initiation of the second and third indents match well the stress level achieved upon unloading of the previous indent. The elastic modulus, obtained from a linear fit between the initiation of unloading to the point of 40% load alleviation, was obtained for each indent using methods typically employed in flat punch nanoindentation experimentation.²¹ Namely

$$E = \frac{\sqrt{\pi}}{2} \frac{S}{\sqrt{A}} \quad (3)$$

where S represents the unloading stiffness of the array and A represents the cross-sectional area of the indenter tip. Because of the low stiffness of the array, deformation of the indentation tip was neglected for this evaluation. The calculated elastic modulus values between 2.6 and 3.3 MPa are slightly less than those previously extracted from similar arrays using nanoindentation in open air,³ perhaps because creep recovery is encouraged by the stepwise nature of the in situ data collection technique or from contributions arising from the vacuum environment, including lack of air within the CNT cellular structure and ambient water vapor, which may tend to enhanced adhesion between neighboring CNTs.

In situ observation of VACNT array nanoindentation reveals that a $7.5\text{ }\mu\text{m}$ tall VACNT array with limited neighboring CNT interactions deflects similarly to a field of classical slender hollow cylinders, while a $600\text{ }\mu\text{m}$ VACNT array with a highly entangled and foam-like morphology produces a cellular buckling response and stress–strain characteristics similar to open-cell foam. The $600\text{ }\mu\text{m}$ array demonstrates evolving deformation regions, with buckle formation first appearing at the bottom of the array, followed by an accumulating buckling front directly under the

indentation tip. The $7.5\text{ }\mu\text{m}$ CNTs exhibit significant elastic recovery, even after 90% compressive strain. Although the $600\text{ }\mu\text{m}$ VACNT array demonstrates full height recovery after application of 7.5% strain, strains of 15% or greater create significant plastic deformation, with most height recovery isolated to the bottom buckle. These direct observations enabled *in situ* nanoindentation provide new insights into the complex deformation mechanisms of beamlike and foam-like CNT arrays and indicate the significant role of array morphology with respect to array deformation.

■ EXPERIMENTAL SECTION

A micromechanical test fixture, shown in Supporting Information (Figure S1), was utilized for the indentation of VACNT arrays. The fixture features a piezoelectric actuator attached in series to a load cell, upon which interchangeable indentation tips may be mounted. The maximum stroke of the piezoelectric actuator is approximately $45\text{ }\mu\text{m}$. A piezoelectric actuated stage is utilized for precise sample positioning with three degrees of freedom. Test fixture control, SEM (FEI Quanta) image acquisition, and data logging is achieved using an external PC running National Instruments LabVIEW software. For optimum SEM image resolution, secondary electron acquisition scans are achieved between displacement intervals during which time the indenter tip position remains static. Telemetric force and displacement data are recorded during each image acquisition period, and the average value of force is reported for each displacement interval. Actuation of the tip is performed at a rate of 100 nm/sec , and each image acquisition requires approximately 90 s. The images may be stitched together to produce a video and synchronized to correlate force and displacement data to the observed deformation phenomena.

The $7.5\text{ }\mu\text{m}$ array was synthesized by pyrolysis of iron(II) phthalocyanine, $\text{FeC}_{32}\text{N}_8\text{H}_{16}$ (FePc, Aldrich) in an Ar/H_2 atmosphere at approximately $1000\text{ }^\circ\text{C}$ in a dual zone tube furnace within a quartz tube.^{11,12} The FePc contains both the carbon source and the metal catalyst. The CNTs synthesized using this procedure have a vertical and relatively straight morphology with an outer diameter of approximately 50 nm and inner diameter of approximately 20 nm . Synthesis of the $600\text{ }\mu\text{m}$ CNT array employed a catalyst film consisting of 3 nm Fe atop 10 nm of Al at $750\text{ }^\circ\text{C}$ and flowing argon, hydrogen, and acetylene gases at $10\text{--}100\text{ Torr}$.¹⁷ The CNTs grown using this procedure had outer diameters between $10\text{--}20\text{ nm}$, with $2\text{--}3$ walls.

■ ASSOCIATED CONTENT

Supporting Information. Schematic and photograph of micromechanical test frame, *in situ* video of $7.5\text{ }\mu\text{m}$ VACNT array indentation, *in situ* videos of $600\text{ }\mu\text{m}$ VACNT array indentation for indent 1, indent 2, and indent 3. This material is available free of charge via the Internet at <http://pubs.acs.org>.

■ AUTHOR INFORMATION

Corresponding Author

*Tel./Fax (937) 255-9072. E-mail: Jeffery.Baur@wpafb.af.mil.

■ ACKNOWLEDGMENT

The authors wish to gratefully acknowledge financial support from the Air Force Office of Scientific Research (AFOSR), Dr. Byung-Lip (Les) Lee, Program Manager and technical assistance from Arthur Safriet during production of a micromechanical sample stage.

■ REFERENCES

- (1) Cao, A.; Dickrell, P. L.; Sawyer, W. G.; Ghasemi-Nejhad, M. N.; Ajayan, P. M. *Science* **2005**, *310* (5752), 1307–13.
- (2) Suhr, J.; Victor, P.; Ci, L.; Sreekala, S.; Zhang, X.; Nalamasu, O.; Ajayan, P. M. *Nat. Nanotechnol.* **2007**, *2* (7), 417–21.
- (3) Maschmann, M. R.; Zhang, Q.; Du, F.; Dai, L.; Baur, J. *Carbon* **2011**, *49* (2), 386–397.
- (4) Zbib, A. A.; Mesarovic, D.; Lilleodden, E. T.; McClain, D.; Jiao, J.; Bahr, D. F. *Nanotechnology* **2008**, *19* (17), 175704.
- (5) Waters, J. F.; Riester, L.; Jouzi, M.; Guduru, P. R.; Xu, J. M. *Appl. Phys. Lett.* **2004**, *85* (10), 1787–1789.
- (6) Hutchens, S. B.; Hall, L. J.; Greer, J. R. *Adv. Funct. Mater.* **2010**, *20* (14), 2338–2346.
- (7) Pathak, S.; Cambaz, G.; Kalidindi, S.; Swadener, G.; Gogotsi, Y. *Carbon* **2009**, *47* (8), 1969–1976.
- (8) Deck, C. P.; Flowers, J.; McKee, G. S. B.; Vecchio, K. J. *Appl. Phys.* **2007**, *101* (2), 23512–1.
- (9) Tong, T.; Zhao, Y.; Delzeit, L.; Kashani, A.; Meyyappan, M.; Majumdar, A. *Nano Lett.* **2008**, *8* (2), 511–15.
- (10) Misra, A.; Greer, J.; Daraio, C. *Adv. Mater. (Weinheim, Ger.)* **2009**, *21* (3), 334–338.
- (11) Qu, L.; Zhao, Y.; Dai, L. *Small* **2006**, *2* (8–9), 1052–1059.
- (12) Huang, S.; Dai, L.; Mau, A. W. H. *J. Phys. Chem. B* **1999**, *103* (21), 4223–4227.
- (13) Zhao, J.; He, M.-R.; Dai, S.; Huang, J.-Q.; Wei, F.; Zhu, J. *Carbon* **2010**, *49* (1), 206–213.
- (14) Min-Feng, Y.; Lourie, O.; Dyer, M. J.; Moloni, K.; Kelly, T. F.; Ruoff, R. S. *Science* **2000**, *287* (5453), 637–40.
- (15) Demczyk, B. G.; Wang, Y. M.; Cumings, J.; Hetman, M.; Han, W.; Zettl, A.; Ritchie, R. O. *Mater. Sci. Eng. A* **2002**, *334* (1–2), 173–178.
- (16) Wong, E. W.; Sheehan, P. E.; Lieber, C. M. *Science* **1997**, *277* (5334), 1971–5.
- (17) Qu, L.; Dai, L.; Stone, M.; Xia, Z.; Wang, Z. *Science* **2008**, *322* (5899), 238–42.
- (18) Bedewy, M.; Meshot, E.; Guo, H.; Verploegen, E.; Lu, W.; Hart, J. *J. Phys. Chem. C* **2009**, *113* (48), 20576–20582.
- (19) Wang, B. N.; Bennett, R. D.; Verploegen, E.; Hart, A. J.; Cohen, R. E. *J. Phys. Chem. C* **2007**, *111* (16), 5859–5865.
- (20) Gibson, L. J.; Ashby, M. F., *Cellular solids: Structure and Properties*; Cambridge University Press: Cambridge, U.K., 1997.
- (21) Fischer-Cripps, A. C. *Nanoindentation*; Springer-Verlag: New York, 2004.